



***ν*bhlight: Radiation GRMHD for Neutrino-driven Accretion Flows**

Jonah M. Miller^{1,2,3} , Ben. R. Ryan^{1,2} , and Joshua C. Dolence^{1,2}

¹ Computational Physics and Methods, Los Alamos National Laboratory, Los Alamos, NM, USA; jonahm@lanl.gov, brryan@lanl.gov, jdolence@lanl.gov

² Center for Theoretical Astrophysics, Los Alamos National Laboratory, Los Alamos, NM, USA

³ Center for Nonlinear Studies, Los Alamos National Laboratory, Los Alamos, NM, USA

Received 2019 January 17; revised 2019 February 20; accepted 2019 February 21; published 2019 April 5

Abstract

The 2017 detection of the in-spiral and merger of two neutron stars was a landmark discovery in astrophysics. We now know that such mergers are central engines of short gamma-ray bursts and sites of *r*-process nucleosynthesis, where the heaviest elements in our universe are formed. In the coming years, we expect many more such mergers. Modeling such systems presents a significant computational challenge along with the observational one. To meet this challenge, we present *ν*bhlight, a scheme for solving general relativistic magnetohydrodynamics with energy-dependent neutrino transport in full (3 + 1) dimensions, facilitated by Monte Carlo methods. We present a suite of tests demonstrating the accuracy, efficacy, and necessity of our scheme. We demonstrate the potential of our scheme by running a sample calculation in a domain of interest—the dynamics and composition of the accretion disk formed by a binary neutron star merger.

Key words: accretion, accretion disks – black hole physics – magnetohydrodynamics (MHD) – methods: numerical – neutrinos – radiative transfer

1. Introduction

We now know that the in-spiral and merger of two neutron stars is a central engine of short gamma-ray bursts (Eichler et al. 1989; Narayan et al. 1992; Soares-Santos et al. 2017) and a site of *r*-process nucleosynthesis (Abbott et al. 2017a), where the heaviest elements in our universe are formed (Lattimer & Schramm 1976; Lattimer et al. 1977; Côté et al. 2018). In the coming years, many more such mergers are expected (Abbott et al. 2017b).

This breakthrough poses a number of questions. What are the dynamics driving the gamma-ray burst? Is the relativistic burst of material out the poles driven by neutrino annihilation (Jaroszynski 1996) or magnetic fields (Blandford & Znajek 1977)? What fraction of these jets escapes, and what fraction is slowed down by ambient material (Mooley et al. 2018)? What fraction of the *r*-process nucleosynthetic yields comes from material in the tidal tails of the merging stars, and what fraction comes from wind driven off of material accreting onto the central remnant (Tanvir et al. 2017)?

This last question is of particular importance for understanding the spectrum of the optical and infrared afterglow of the merger event (Tanvir et al. 2017). The heavy elements produced via *r*-process nucleosynthesis radioactively decay, producing this afterglow—the so-called macronova or kilonova (Lattimer & Schramm 1976; Lattimer et al. 1977; Blinnikov et al. 1984; Li & Paczyński 1998; Metzger et al. 2010; Côté et al. 2018). The remnant accretion disk ejects mass as a wind, which may be thermal, magnetically driven, or neutrino driven.⁴ Along with the tidal tails in the merger, this wind may be one site of *r*-process nucleosynthesis.

The dynamics of the *r*-process in the wind depend on its composition, which depends on the lepton number, and thus neutrino processes and transport. The mass and morphology of the wind depends on the dynamics of the disk, which depends on magnetically driven turbulence via the magneto-rotational

instability (Balbus & Hawley 1991), neutrino transport, and general relativistic effects, such as frame dragging (Wald 2010). Therefore, accurately computing the nucleosynthetic yields produced—and thus the spectrum of the kilonova—depends sensitively on the interplay of gravity, plasma physics, and neutrino radiation transport. In other words, they are well-modeled by general relativistic radiation magnetohydrodynamics (GRRMHD).

Although black hole accretion disk physics is a large and well-explored topic,⁵ very few three-dimensional (3D) calculations of accretion disks formed by a compact binary merger including neutrino physics have been performed, and those have only been recently. (Indeed, few GRRMHD simulations of disks have been performed in any context.) Sekiguchi et al. (2015) used a hybrid leakage-moment scheme to model the radiation in a binary neutron star merger and followed the accretion disk formed post-merger. Foucart et al. (2015) and Hossein Nouri et al. (2018) used a moment method to treat the radiation in a disk formed by the merger of a black hole and a neutron star. Siegel & Metzger (2018) modeled a disk formed by the merger of two neutron stars with general relativistic magnetohydrodynamics on a Cartesian grid and a leakage scheme for the neutrinos. Siegel et al. (2018) use a similar calculation to argue that *r*-process nucleosynthesis can occur in disks formed by the collapse of massive stars. Fernández (2019) performed a suite of studies of the disk outflow with a cooling function treatment for the neutrino physics.

These groundbreaking efforts, although heroic, make significant approximations in the treatment of the radiation transport. Realistic modeling of neutrino transport requires solving the (6 + 1)-dimensional kinetic Boltzmann equation for each neutrino species, which is computationally expensive and numerically challenging. In the limit of infinite optical depth, the radiation field may be treated with diffusion physics—see, e.g., Miralles et al. (1993). For vanishing optical depth, a cooling or leakage scheme, where neutrinos are allowed to

⁴ Fernández & Metzger (2016) and references therein offer a nice summary of these processes.

⁵ See Abramowicz & Fragile (2013) and references therein for a review.

freely stream through material, is appropriate. Indeed this is the approach taken by Siegel et al. (2018) and Fernández (2019). For intermediate optical depths, the transport equations must be solved directly. Moment-based schemes, where the continuum limit of the radiation field is taken and a set of hydrodynamic-like equations are attained, sidestep this requirement by imposing strong assumptions on the radiation field in order to close the system of equations, with poorly understood consequences on modeling accuracy. This approach was used by Foucart et al. (2015) and Hossein Nouri et al. (2018).⁶

We seek to the remedy this gap. We present *νbhlight*, a new GRRMHD code with accurate neutrino transport via Monte Carlo methods. Monte Carlo methods solve the full kinetic Boltzmann equation, discretized with particles, each of which represents a packet of radiation. *νbhlight* is built on the successful photon GRRMHD code *bhlight* (Ryan et al. 2015) and is designed specifically to tackle the post-merger disk problem.

In Section 2, we describe in detail the system of equations *νbhlight* is designed to solve. In Section 3, we describe the methods used. In Section 4, we describe code tests used to verify *νbhlight*. In Section 5, we demonstrate our new capabilities with an example calculation of a post-merger disk in full 3D with realistic neutrino transport. Finally, in Section 6, we offer some concluding thoughts.

2. System

We solve the equations of relativistic ideal MHD coupled to neutrino radiation. We use a formulation almost identical to that presented in Gammie et al. (2003), Dolence et al. (2009), and Ryan et al. (2015). However, there are a few key differences. We evolve the conserved lepton number density (encapsulated in the electron fraction Y_e). Unlike Gammie et al. (2003), this necessitates a realistic, tabulated equation of state (EOS). Unlike in Dolence et al. (2009) and Ryan et al. (2015), our radiation is relativistic neutrinos, not photons. Our radiation sector carries a conserved lepton number, as well as energy and momentum. Moreover, while there is only one “type” of photon, there are several flavors of neutrinos, which we bundle into three types: electrons, anti-electrons, and heavies. We discuss the details of these differences below.

2.1. Fluid

The fluid sector consists of the following system of equations:

$$\partial_t(\sqrt{-g} \rho_0 u^t) + \partial_i(\sqrt{-g} \rho_0 u^i) = 0 \quad (1)$$

$$\partial_t[\sqrt{-g}(T_\nu^t + \rho_0 u^t \delta_\nu^t)] + \partial_i[\sqrt{-g}(T_\nu^i + \rho_0 u^i \delta_\nu^t)] \\ = \sqrt{-g}(T_{\lambda\nu}^\lambda \Gamma_{\nu\kappa}^\lambda + G_\nu) \quad \forall \nu = 0, 1, \dots, 3 \quad (2)$$

$$\partial_t(\sqrt{-g} B^i) - \partial_j[\sqrt{-g}(b^j u^i - b^i u^j)] = 0 \quad (3)$$

$$\partial_t(\sqrt{-g} \rho_0 Y_e u^t) + \partial_i(\sqrt{-g} \rho_0 Y_e u^i) = \sqrt{-g} G_{ye}, \quad (4)$$

where the energy-momentum tensor T_ν^μ is assumed to be

$$T_\nu^\mu = (\rho_0 + u + P + b^2) u^\mu u_\nu + \left(P + \frac{1}{2} b^2\right) \delta_\nu^\mu - b^\mu b_\nu \quad (5)$$

for metric $g_{\mu\nu}$, rest energy ρ_0 fluid four-velocity u^μ , internal energy density u , pressure P , and Christoffel connection $\Gamma_{\beta\gamma}^\alpha$.

Equation (1) represents conservation of the baryon number. Equation (2) represents conservation of energy-momentum, which is subject to the radiation four-force G_ν (not to be confused with the Einstein tensor). Note that we have added a multiple of Equation (1) to the $\nu = 0$ index of the canonical form of the energy-momentum equation to arrive at Equation (2). This is equivalent to the canonical form, but removes rest energy from the energy conservation law. We found this approach to be more numerically favorable. See Martí et al. (1991) for one influential work that uses this trick.

Equation (3) describes the evolution of magnetic fields, where

$$B^i = {}^*F^{it} \quad (6)$$

comprises the magnetic field components of the Maxwell tensor $F_{\mu\nu}$, and b^μ is the magnetic field four-vector:

$${}^*F^{\mu\nu} = b^\mu u^\nu - b^\nu u^\mu. \quad (7)$$

Finally, Equation (4) describes the conservation of the lepton number. G_{ye} is a source term describing the rate at which lepton density is transferred between the fluid and the radiation field. It will be described in more detail below.

The system is closed by an EOS, which relates the pressure P to the density ρ , internal energy u , and electron fraction Y_e :

$$P = P(\rho, u, Y_e). \quad (8)$$

We use an equivalent, temperature-dependent formulation of the EOS which relates the pressure P and specific internal energy $\varepsilon = u/\rho$ to the density ρ , temperature T , and electron fraction Y_e :

$$P = P(\rho, T, Y_e) \quad (9)$$

$$\frac{u}{\rho} := \varepsilon = \varepsilon(\rho, T, Y_e). \quad (10)$$

We invert Equation (10) to find the temperature and then calculate the pressure using Equation (9).

2.2. Neutrino Physics

We are interested in r -process nucleosynthesis, which depends on the fraction of free neutrons in our gas, or

$$1 - Y_e.$$

The electron fraction Y_e is affected by the emission or absorption of electron neutrinos (denoted ν_e) and electron antineutrinos (denoted $\bar{\nu}_e$) but is unaffected by the emission and absorption of all other neutrinos. We, therefore, dub the other neutrinos, which do not modify electron number heavy neutrinos and denote them ν_x . If neutrino species does not matter (or we wish to iterate over species, depending on the context), we denote the neutrinos as ν_i .

We include many different interactions of neutrinos with matter. We categorize these processes as “absorption or emission” and as “scattering” processes. We list the absorption and emission processes in Table 1. Those that involve the absorption or emission of an electron neutrino or antineutrino can change the electron fraction and therefore the number of free neutrons in the gas. We include the elastic scattering

⁶ Much progress has also been made in the postprocessing of simulations of accretion disks with realistic transport. See, for example, Richers et al. (2015) and Foucart (2018).

Table 1
Emission and Absorption Processes Used in *νbhlight*

Type	Processes	Charged/Neutral	Corrections/Approximations
Abs./Emis. on neutrons	$\nu_e + n \leftrightarrow e^- + p$ $\nu_\mu + n \leftrightarrow \mu^- + p$	Charged	Blocking/Stimulated abs. weak magnetism recoil
Abs./Emis. on protons	$\bar{\nu}_e + p \leftrightarrow e^+ + n$ $\bar{\nu}_\mu + p \leftrightarrow \mu^+ + n$	Charged	Blocking/Stimulated abs. weak magnetism recoil
Abs./Emis. on ions	$\nu_e A \leftrightarrow A' e^-$	Charged	Blocking/Stimulated abs. recoil
Electron capture on ions	$e^- + A \leftrightarrow A' + \nu_e$	Charged	Blocking/Stimulated abs. recoil
$e^+ - e^-$ annihilation	$e^+ e^- \leftrightarrow \nu_i \bar{\nu}_i$	Charged + neutral	Single- ν blocking recoil
$n_i - n_i$ Bremsstrahlung	$n_i^1 + n_i^2 \rightarrow n_i^3 + n_i^4 + \nu_i \bar{\nu}_i$	Neutral	Single- ν blocking recoil

Note. The symbols in the processes are as follows: n is a neutron, p is a proton, e^- is an electron, e^+ is a positron, μ^- is a muon, μ^+ is an antimuon, and n_i is an arbitrary nucleon. ν_i is an arbitrary neutrino. ν_e is an electron neutrino, and $\bar{\nu}_e$ is an electron antineutrino. We describe the corrections and approximations used below, as tabulated in Skinner et al. (2019) and provided to us in A. Burrows (2018, private communication). Blocking and stimulated absorption are related to the Fermi–Dirac nature of neutrinos. Weak magnetism is related to the extended quark structure of nucleons. Recoil is the kinematic recoil. Single- ν blocking is a Kirkhoff’s law based approximation of blocking that becomes exact for processes that involve only a single neutrino. The details of these interactions are summarized in Burrows et al. (2006).

processes listed below:

$$\nu_i + p \leftrightarrow \nu_i + p \quad (11)$$

$$\nu_i + n \leftrightarrow \nu_i + n \quad (12)$$

$$\nu_i + A \leftrightarrow \nu_i + A \quad (13)$$

$$\nu_i + \alpha \leftrightarrow \nu_i + \alpha \quad (14)$$

where n represent neutrons, p represents protons, ν_i represents neutrinos of arbitrary type, A represents heavy ions, and α represents alpha particles.

There are several effects that we are neglecting, mainly inelastic scattering of neutrinos off of electrons (Bruenn 1985); neutrino–neutrino annihilation, which may help drive the gamma-ray burst (Eichler et al. 1989); and neutrino oscillations (Duan et al. 2011). We also neglect ion screening, electron polarization, and form factor corrections to neutrino-heavy ion scattering (Equation (13)). Although this effect is subdominant in core-collapse supernovae (Bruenn & Mezzacappa 1997), we do not know how important it is for the disk problem. We also note that the pair processes, i.e., nucleon–nucleon bremsstrahlung and particle–antiparticle annihilation, do not impose any conditions on pairs of Monte Carlo radiation packets. Rather, they are approximated as isotropic processes and incorporated into our emissivities and absorption opacities. On large scales, i.e., GM_{BH}/c^2 for a black hole of mass M_{BH} , we believe this is a good approximation. Since this work is a “first pass” at accurately tracking neutrino physics in neutrino-driven accretion flows, we believe ignoring these effects initially is justified. We will incorporate and study them in future work.

Neutrino interactions with matter have a long history in astrophysics (Freedman 1974; Tubbs & Schramm 1975; Fuller et al. 1982; Bruenn 1985; Leinson et al. 1988; Aufderheide et al. 1994; Horowitz 1997). We borrow these results to produce our emissivities, opacities, and cross sections. Our emissivities and opacities in particular are drawn from tabulated data first presented in Burrows et al. (2006), which also accounts for subdominant high-density many-body effects. Scattering is treated on an interaction-by-interaction basis, and we use analytic single-particle cross sections. We use cross sections as summarized in Burrows et al. (2006).

2.3. Treatment of the Neutrino Radiation Field

We assume our neutrinos are massless, travel on null geodesics, and obey a light-like dispersion relation

$$-k^\mu \eta_\mu = \epsilon = h\nu, \quad (15)$$

where h is Planck’s constant, and ϵ is the energy of a neutrino with wavevector k^μ as measured by an observer traveling along a timelike Killing vector η^μ . Here, ν is the frequency of the neutrino. However, to avoid notational confusion, we will usually use ϵ rather than ν when referring to neutrino energies and frequencies, which are interchangeable via a factor of Planck’s constant. Since the neutrino mass is both small and unknown—far smaller than the many MeV energy neutrinos attained in post-merger disks—we believe this is a reasonable approximation.

We thus recast our neutrino transport as the standard radiative transfer equation

$$\frac{D}{d\lambda} \left(\frac{h^3 I_{\epsilon f}}{\epsilon^3} \right) = \left(\frac{h^2 \eta_{\epsilon f}}{\epsilon^2} \right) - \left(\frac{\epsilon \chi_{\epsilon f}}{h} \right) \left(\frac{h^3 I_{\epsilon f}}{\epsilon^3} \right), \quad (16)$$

where $D/d\lambda$ is a derivative along a neutrino trajectory in phase space, $I_{\epsilon f}$ is the intensity of the neutrino field of flavor $f \in \{\nu_e, \bar{\nu}_e, \nu_x\}$,

$$\chi_{\epsilon f} = \alpha_{\epsilon f} + \sigma_{\epsilon f}^a \quad (17)$$

is the extinction coefficient that combines absorption coefficient $\alpha_{\epsilon f}$ and scattering extinction $\sigma_{\epsilon f}^a$ for scattering interaction a , and

$$\eta_{\epsilon f} = j_{\epsilon f} + \eta_{\epsilon f}^s(I_{\epsilon f}) \quad (18)$$

is the emissivity combining fluid emissivity $j_{\epsilon f}$ and emission due to scattering from $\eta_{\epsilon f}^s$. Note that every neutrino flavor has its own radiation field and interactions with matter. (Equivalently, the radiation field has an extra, discrete index specifying neutrino flavor.) Each of the quantities in Equation (16) is invariant.

2.4. Radiation-fluid Interactions

We define an orthonormal tetrad⁷

$$e_{(a)}^\mu$$

with

$$e_{(a)}^\mu e_{(b)}^\nu = \eta_{ab}^{\mu\nu} \quad (19)$$

so that

$$e_{(i)}^\mu = u^\mu, \quad (20)$$

i.e., so that it is comoving with the fluid. In this frame, the radiation four-force is

$$G_{(a)} = \frac{1}{h} \int d\epsilon d\Omega (\chi_{\epsilon f} I_{\epsilon f} - \eta_{\epsilon f}) n_{(a)}, \quad (21)$$

where $n_{(a)} = p_{(a)}/\epsilon$. A coordinate transformation then maps the comoving radiation four-force into the lab frame:

$$G^\mu = e_{(a)}^\mu G^{(a)}. \quad (22)$$

The scalar source term G_{ye} for lepton conservation (Equation (4)) is similar. When evaluated in the fluid frame, it is given by

$$G_{ye} = \frac{m_p}{h} \text{sign}(f) \int \frac{\chi_{\epsilon f} I_{\epsilon f} - \eta_{\epsilon f}}{\epsilon} d\Omega d\epsilon, \quad (23)$$

where m_p is the mass of a proton and

$$\text{sign}(f) = \begin{cases} 1 & \text{if } f = \nu_e \\ -1 & \text{if } f = \bar{\nu}_e \\ 0 & \text{if } f = \nu_x \end{cases} \quad (24)$$

determines the sign of the contribution.

3. Methods

3.1. Fluid Integration

We evolve our fluid via a standard second-order conservative high-resolution shock capturing finite volume method. We base our implementation in this sector on the High-Accuracy Relativistic Magnetohydrodynamics (HARM) code (Gammie et al. 2003) and use the same set of primitive and conserved variables as described in Gammie et al. (2003) and Ryan et al. (2015), with the lone exception being the electron fraction. We describe our implementation of the electron fraction in more detail in Section 3.3.

We use a local Lax–Friedrichs approximate Riemann solver (Harten et al. 1983). For reconstructions, we use either a linear reconstruction with a monotized central slope limiter (Toro 2013) or a fifth-order weighted essentially non-oscillatory (WENO) reconstruction (Liu et al. 1994). The form we use is the variant described in Tchekhovskoy et al. (2007), although we do not manually reduce the order of reconstruction near discontinuities.

We treat our magnetic fields via a constrained transport method described by Tóth (2000). This version of constrained transport uses cell-centered magnetic fields. We use a special second-order derivatived operator that ensures that a discrete, corner-centered divergence of the magnetic field vanishes. Since this scheme uses centered-differencing, it neglects

electromagnetic force (emf) upwinding, which can be important for flux loop advection. For more details, see Gammie et al. (2003).

In general relativity, the conversion between conserved variables and primitive variables is not known analytically and involves the numerical root finding of a complex algebraic function. We use the procedure described by Mignone and McKinney in Mignone & McKinney (2007).

3.2. Radiation Transport

We modified the way `bhlight` performs radiation transport. We transport three types of radiation packet, each one corresponding to electron neutrinos, electron antineutrinos, or heavy neutrinos. Each type of neutrino has separate emissivities and opacities. This implies that the probability that a given radiation packet is emitted, scattered, or absorbed depends on the neutrino type. There are two ways we could account for this:

1. Treat each neutrino type as a separate class of radiation objects and draw probabilities from completely separate probability distributions, one for each neutrino type.
2. Draw probabilities from a joint probability distribution, which depends on the neutrino type.

The former allows for more fine-grained control over how phase space is sampled, while the latter has the advantage of being simpler to implement. Because of its simplicity, we have implemented option 2. We now describe this approach in more detail. Our treatment closely follows that in Dolence et al. (2009) with a few modifications. Here, we emphasize the differences between our algorithm and that described in Dolence et al. (2009) and Ryan et al. (2015).

3.2.1. Emissivity

The probability distribution of emitted radiation packets is given by

$$\frac{1}{\sqrt{-g}} \frac{dN_s}{d^3x dt dv d\Omega} = \frac{1}{w \sqrt{-g}} \frac{dN}{d^3x dt dv d\Omega} = \frac{1}{\omega} \frac{j_{\epsilon f}}{h\nu}, \quad (25)$$

where N_s is the number of “superneutrinos,” or radiation packets with w physical neutrinos per packet, N is the number of physical neutrinos, $j_{\epsilon f}$ is the emissivity (in the plasma frame) of neutrinos of species i with de Broglie frequency ν and flavor $f \in \{\nu_e, \bar{\nu}_e, \nu_x\}$, and h is Planck’s constant.

This implies that the number of superneutrinos created in a time interval Δt is

$$N_{s,\text{tot}} = \Delta t \sum_{f \in \{\nu_e, \bar{\nu}_e, \nu_x\}} \int \sqrt{-g} d^3x dv d\Omega \frac{1}{w} \frac{j_{\epsilon f}}{h\nu}, \quad (26)$$

and the number of superneutrinos of flavor f created in a finite volume cell i of volume Δ^3x is given by

$$N_{s,if} = \Delta t \Delta^3x \int \sqrt{-g} dv d\Omega \frac{1}{w} \frac{j_{\epsilon f}}{h\nu}. \quad (27)$$

We approximately fix the total number of superneutrinos created per time step by setting the weight w .

We set the weight to

$$w = \frac{C}{\nu}, \quad (28)$$

⁷ Here, roman Greek indices indicate a lab frame, and Latin indices in parentheses indicate a comoving frame.

where C is a constant.

This ensures that a superneutrino of frequency ν and $w(\nu)$ has a total energy of

$$E_s = wh\nu = hC; \quad (29)$$

superneutrino energy is independent of frequency.

We calculate the constant C by fixing the total number of superneutrinos created to be N_{target} and inverting Equation (26) for C . We decide N_{target} by trying to keep the total number of superneutrinos constant over time. This means N_{target} is chosen so that the superneutrinos created and scattered replace those lost to absorption or that leave the domain. This results in the integral quantity:

$$C = \frac{\Delta t}{hN_{\text{target}}} \sum_{f \in \{\nu_e, \nu_\mu, \nu_\tau\}} \int \sqrt{-g} d^3x dv d\Omega j_{ef}. \quad (30)$$

To summarize, in order to produce superneutrinos, we sample them from a species dependent probability distribution that has a weight calculated by integrating over the total probability distribution for all species.

3.2.2. Absorption

Our treatment of absorption is identical to that described in Ryan et al. (2015), except that absorption extinction coefficients are now evaluated per neutrino species. Absorption is treated probabilistically. If a radiation packet of neutrino flavor f travels an affine distance $\Delta\lambda$, it passes through an incremental optical depth to absorption:

$$\Delta\tau_a(\nu, f) = \nu\alpha_{ef}\Delta\lambda, \quad (31)$$

where α_{ef} is the absorption extinction coefficient for neutrino radiation of flavor f and frequency ν . An absorption event occurs if

$$\Delta\tau_a(\nu, f) > -\ln(r_a), \quad (32)$$

where r_a is a random variable sampled uniformly from the interval $[0, 1)$.

3.2.3. Scattering

Like in `bhlight`, scattering in `νbhlight` is treated probabilistically. We generalize the approach in `bhlight` to treat the scattering of radiation off of multiple scattering particles, each with their own cross section. We allow our neutrinos to scatter elastically off of protons (Equation (11)), neutrons (Equation (12)), heavy nuclei (Equation (13)), and alpha particles (Equation (14)). We calculate the individual number densities of the constituent particles via the appropriate mass fraction, which is tabulated in our equations of state.

For each neutrino flavor f and type p of gas particle off of which a neutrino can scatter, we construct a scattering extinction coefficient, $\alpha_s(\nu, f, p)$. Then, a superneutrino of flavor f scatters off of a particle of species p if

$$\Delta\tau_p(f) > -\ln(r_s)/b_s(\nu, f, p), \quad (33)$$

where $\Delta\tau_p(f)$ is the scattering optical depth due to an interaction between the neutrino and the particle, constructed analogously to the absorption optical depth (Equation (31)), and $b_s(\nu, f, p)$ is a bias parameter that enhances the probability of scattering. To ensure that the biased process reflects nature, we reset the weight of the scattered superneutrino to w/b for a

conservative process with the incident superneutrino of weight w . For more details, see Dolence et al. (2009) and Ryan et al. (2015).

How do we sample multiple different interactions? After all, the neutrino should be subject to absorption and scattering against all kinds of particles. When a superneutrino travels an affine distance of $\Delta\lambda$, we construct all optical depths,

$$\{\Delta\tau_i\}_{i \in \{a, p\}},$$

and biases,

$$\{b_i\}_{i \in \{a, p\}},$$

for absorption and scattering against all particles. Then, we sample a uniform random variable,

$$r_i, i \in \{a, p\},$$

for each type of interaction. The interaction that occurs is the one for which the ratio,

$$-\frac{\ln(r_i)}{b_i \Delta\tau_i}, \quad (34)$$

is smallest for all $i \in \{a, p\}$.

Unlike in Dolence et al. (2009) and Ryan et al. (2015), we allow our bias parameters to depend individually on both the neutrino flavor f and the species of interacting particle p . In particular, we demand that the parameter

$$b_s(\nu, f, p) \Delta\tau_p(f) \quad (35)$$

be approximately equal for all scattering processes. This ensures that all scattering processes are equally well sampled. In Section 4.5, we provide evidence that this procedure is both necessary and effective.

3.2.4. Sampling the Scattered Superneutrino

To generate a new superneutrino from an incident one with wavevector k^μ , we follow a modified version of the procedure presented in Dolence et al. (2009) and Ryan et al. (2015):

1. We boost into the rest frame of the plasma.
2. We sample the four-momentum p^μ of the particle off of which the superneutrino scatters from a thermal relativistic Maxwell distribution using the procedure described in Canfield et al. (1987). Note that this requires the differential single-particle cross section for the interaction of the scattering particle with the neutrino.
3. We boost into the rest frame of the scattering particle.
4. We sample the wavevector k_s^μ of the scattered superneutrino from the differential single-particle cross section.
5. We transform k_s^μ back into the lab frame.

This is why we must perform scattering on a per scatterer basis. Otherwise, the differential cross section is inaccessible.

3.2.5. Radiation Force

We calculate the radiation four-force on the fluid by conserving four-momentum, in a manner identical to that described in Ryan et al. (2015). The only complication emerges from the tracking of the lepton number.

3.2.6. Tracking Lepton Number

When a superneutrino is emitted or absorbed, it can modify the electron fraction of the gas. We couple this contribution to the electron fraction evolution via an operator split update analogous to the radiation four-force update in Ryan et al. (2015). The emission of a neutrino radiation packet of flavor f and weight w provides a discrete contribution to source term (Equation (23)) of magnitude

$$\frac{\Delta(\sqrt{-g}\rho u^0 Y_e)}{\Delta t} = -\sqrt{-g} \frac{w u^0 m_b}{\sqrt{-g} \Delta^4 x} \text{sign}(f), \quad (36)$$

where u^0 is the time component of the fluid four-velocity, m_b is unit mass per baryon in the gas, and $\sqrt{-g} \Delta^4 x$ is the invariant four-volume of a discrete finite-volume cell (including the time step). The contribution to this source term for absorption is equal and opposite.

3.2.7. A Note on Time Steps

We pause briefly to note limits on the size of our time step. Our method is fully explicit, both in the radiation and fluid sectors. We feel comfortable applying a fully explicit approach because the systems we are interested in have modest optical depths, and cooling times are long. Moreover, our approach to scattering and absorption requires that a superneutrino does not travel more than one cell distance in one time step. This time-step restriction means that the restriction on the time step due to using a fully explicit approach that is not so severe.

We, therefore, insist that our time step is smaller than the following quantities:

1. The light-crossing time within any cell.
2. The cooling time due to emissivity, $u / \int d\nu d\Omega j_\nu$.

The emissivity condition (2) is not a guarantee for stability. Rather, it is a guarantee that the system will converge to a stable solution in the limit of a large superneutrino number. In practice, we find that the light-crossing time within a cell is almost always the smallest of these quantities, and the cooling time restriction is not severe.

3.3. Advection and Passive Scalars

As discussed in Section 2, the electron fraction Y_e evolves via Equation (4). We have implemented a generic framework for evolving variables that are “passively” advected by the fluid, i.e., so-called passive variables. Our framework allows for two methods of advection, which differ by what variable is considered the primitive variable. We dub these two approaches advect intrinsics and advect numbers.

3.3.1. Advecting Intrinsics

An extrinsic thermodynamic quantity is one that grows linearly with volume. Extrinsic quantities include total energy and entropy. An intrinsic quantity is the corresponding extrinsic quantity per volume. This is in contrast to, say, specific quantities, which are extrinsic quantities per mass.

Consider an intrinsic variable ϕ that is passively advected by the fluid. It obeys the differential equation

$$(\phi u^\mu)_{;\mu} = 0, \quad (37)$$

where u^μ is the fluid four-velocity. If we perform a $(3 + 1)$ split and translate this into the language of finite volumes, ϕ is our primitive variable, ϕu^0 is our conserved variable, and ϕu^i is our flux in the i th direction. If

$$\phi = \rho Y_e, \quad (38)$$

then we recover Equation (4) for conservation of the lepton number.

3.3.2. Advecting Numbers

Consider a “number” quantity X , which is neither intrinsic nor extrinsic. The “density” $X\rho$ will be intrinsic. This fact suggests an alternative form of Equation (37):

$$(X\rho u^\mu)_{;\mu} = 0, \quad (39)$$

where the conserved variable is now $X\rho u^0$ and the i th flux is $X\rho u^i$. However, there is a degeneracy in the primitive variable. If we treat $X\rho$ as the primitive, we recover the formalism in Section 3.3.1. If we treat X as the primitive, we recover a mathematically equivalent but numerically distinct approach. This is the advect numbers scheme.

If $X = Y_e$, then Equation (39) becomes Equation (4) for the conservation of the lepton number. In practice, we have found that advecting Y_e as a number as per Equation (39) to be more numerically robust—particularly in the atmosphere—than advecting the conserved proton mass density as per Equation (37), and this is the approach we use.

3.4. Equation of State

We have implemented realistic, tabulated nuclear equations of state. We use the tables as generated and described in O’Connor & Ott (2010a, 2010b). Our EOS tables provide thermodynamic quantities in terms of the log of the density, $\log_{10} \rho$; the log of the temperature, $\log_{10} T$; and the electron fraction, Y_e .

Since temperature is not one of our primitive (or conserved) variables, we must solve for it via a 1D root finding. In our implementation, we use Newton’s method but default to a bisection if Newton’s method fails. To do so, we invert the relation

$$\rho \varepsilon(\log_{10} \rho, \log_{10} T, Y_e) = u \quad (40)$$

with a given specific internal energy ε or the relation

$$\begin{aligned} \rho &= w(\log_{10} \rho, \log_{10} T, Y_e) \\ &\quad - \rho \varepsilon(\log_{10} \rho, \log_{10} T, Y_e) \\ &\quad - P(\log_{10} \rho, \log_{10} T, Y_e) \end{aligned} \quad (41)$$

with a given enthalpy by volume w for $\log_{10} T$, where $\log_{10} \rho$ and Y_e are given by the primitive state. We can then extract thermodynamic quantities, such as pressure and sound speed. (We use Equation (41) when solving for our primitive variables from our conserved variables and Equation (40) everywhere else.)

3.5. Atmosphere Treatment

Equations (1), (2), and (4) are valid only for nonvanishing density ρ . Moreover, only some values of internal energy u and electron fraction Y_e are physically valid. Therefore, we must

impose floors on these quantities to keep them in a physically valid regime.

An additional complication is that tabulated thermodynamic values are available only for a finite range of temperatures, pressure, and electron fractions:

$$\begin{aligned} \log_{10} \rho &\in [\log \rho_{\min}, \log \rho_{\max}] \\ \log_{10} T &\in [\log T_{\min}, \log T_{\max}] \\ \text{and } Y_e &\in [(Y_e)_{\min}, (Y_e)_{\max}]. \end{aligned} \quad (42)$$

Therefore, these limits must be accounted for in some way. The physically allowed values of the electron fraction sit well within the range given by Equation (42), so we simply set floors and ceilings for the electron fraction given by $(Y_e)_{\min}$ and $(Y_e)_{\max}$.

For density in black hole metrics, we demand that

$$\rho \geq \rho_{\text{flr}} = \frac{\rho_0}{r^2}, \quad (43)$$

where we choose $\rho_0 \approx 10^{-5}$ for our disk simulations.⁸ This implies that near the black hole, our floor is about 10^{-5} in code units.⁹ However, the floor decays in the radius, so it is much smaller at large radii. This treatment is designed to ensure that the atmosphere does not interfere with diffuse winds blown off the disk.

For these large radii, $\rho_{\text{flr}} < \log \rho_{\min}$. We, therefore, analytically extend the table with a cold, polytropic EOS (which depends on electron fraction),

$$P_{\text{poly}} = K(Y_e) \rho^{\Gamma(Y_e)}, \quad (44)$$

where K and Γ are chosen so that P_{poly} and $(\partial P_{\text{poly}} / \partial \rho)_s$ match the table at $(\log \rho_{\min}, \log T_{\min}, Y_e)$.

For internal energy u , we demand that

$$u \geq u_{\text{flr}}(Y_e) = \rho_{\text{flr}} \varepsilon(\rho_{\text{flr}}, \log T_{\min}, Y_e), \quad (45)$$

where the specific internal energy ε can contain contributions from binding energy and can thus be negative. For consistency with the cold nature of the polytropic EOS (Equation (44)), we set $u = u_{\text{flr}}$ when ρ is less than some threshold value, typically a $\log \rho_{\min} / 10^5$ or less. In magnetically dominated regions, these floors are imposed in the rest frame of the fluid. However, in matter- or kinetic energy-dominated regions, they are imposed in the lab frame.

We note that our treatment of the floors is not thermodynamically consistent. Moreover, any application of density floors is unphysical and can, if care is not taken, change the results of a simulation. Unfortunately, within an Eulerian framework, we have no choice but to apply density floors. Fortunately, this inconsistency affects only very-low-density regions and should, therefore, not change the results of a simulation if used judiciously. We have experimented with floor values and found the results of our simulations to be insensitive to these choices.

Electron fraction has no meaning in the atmosphere, but numerically, we must set it to something. For simplicity, we set the atmosphere to have an electron fraction of $Y_e = 0.5$ at the initial time. When density floors are enforced, Y_e is not reset. Rather, the bounds on Y_e are enforced independently.

3.6. Tracer Particles

We added tracer particles to *νbhlight*. A tracer particle is a numerical representation of a Lagrangian fluid packet, which is passively advected with the fluid. In the $(3 + 1)$ split of general relativity, tracers obey the equation of motion:

$$\frac{dx^i}{dt} = \frac{u^i}{u^0} = \alpha v^i - \beta^i, \quad (46)$$

where x^i are the spatial components of the tracer's position vector, α is the lapse, β^i is the components of the shift, v^i is the three-velocity of the fluid, and u^μ is the four-velocity of the fluid (Foucart et al. 2014).

We interpolate the velocities in Equation (46) via second-order Lagrange interpolation. The tracers are integrated in time via a second order explicit Runge–Kutta scheme and, because we integrate them in lockstep with the fluid, the coupling between tracers and fluid is fully second order. We utilize the particle infrastructure already implemented in *νbhlight* to treat tracers with the same shared and distributed memory parallelism as that for superneutrinos.

In this work, we follow Bovard & Rezzolla (2017) and roughly uniformly sample our tracers everywhere where there is physical fluid (i.e., everywhere that is not atmosphere). When we set up a disk, for each cell containing disk material, we calculate the total mass within the cell, and equally distribute it between N tracer particles that are placed in the cell. The tracer positions within the cell are randomly sampled from the uniform distribution.

4. Code Verification

Many aspects of *νbhlight* have been tested rigorously in previous works, such as Gammie et al. (2003), Dolence et al. (2009), and Ryan et al. (2015). Here, we discuss tests of the added functionality required to study neutrino transport.

4.1. Advection Tests

To test the passive scalar framework described in Section 3.3, we study the advection of an intrinsic (in the thermodynamic sense) scalar field by a constant (in space and time) fluid flow in flat Minkowski space. Under these conditions and in one spatial dimension, Equation (37) reduces to¹⁰

$$\partial_t \phi + \frac{u^x}{\sqrt{1 - (u^x)^2}} \partial_x \phi = 0, \quad (47)$$

where u^x is the velocity of the fluid in the x -direction in Minkowski coordinates.

We solve Equation (47) as an initial value problem using the techniques described in Section 3.1 with the initial conditions

$$\phi_0(t = 0, x) = \begin{cases} 4x^2 & \text{if } x \leq 0 \\ 0 & \text{otherwise} \end{cases} \quad (48)$$

$$\text{and } \phi_1(t = 0, x) = A \sin(2\pi x) \quad (49)$$

for scalar fields ϕ_0 and ϕ_1 , with both obeying Equation (47) and with periodic boundary conditions on the domain $x \in [-1, 1]$.

⁸ This choice is problem dependent.

⁹ Typically, it is approximately 10^5 g cm^{-3} in physical units.

¹⁰ Here, although we describe the problem setup for the advection of intrinsic variables, the test (and results) for advection of numbers is identical.

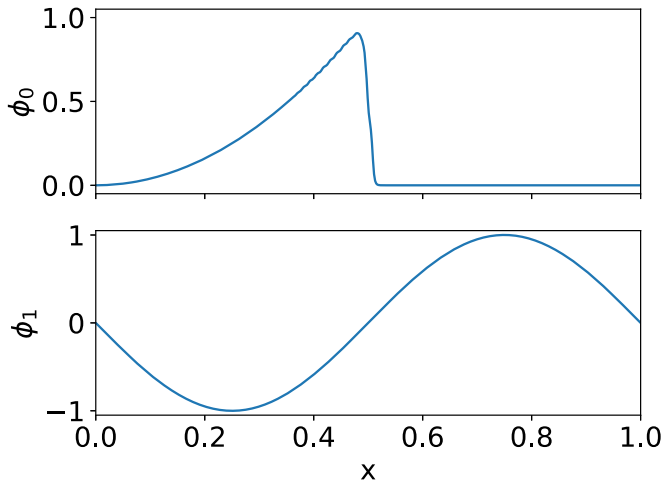


Figure 1. Solution to Equation (47) given initial data Equations (48) and (49) with periodic boundaries after one cycle.

We plot a solution to this initial-boundary value problem at $t = 2\sqrt{1 - (u^x)^2}/u^x$ in Figure 1.

We use Equation (49) to check for convergence and Equation (48) to test the handling of discontinuities. A 3D version of this test can be constructed by rotating initial data Equation (49) by 45° about the y - and z -axes. We plot a 2D slice of ϕ_1 in the 3D test in Figure 2 and a 2D slice of the pointwise error in Figure 3. Finally, we plot the convergence of the infinity norm of the error in ϕ_1 in 3D in Figure 4. As expected for a second-order Godunov-type method, our solution converges at the second order.

4.2. Tracer Particles

We test the tracer particle infrastructure described in Section 3.6 by constructing known fluid flows and by watching the tracers advect with the fluid.

4.2.1. Advection

One simple known flow is that given by Equation (47) in Section 4.1. In this case—where the velocity field is uniform and constant in time—there is no truncation error in the spatial discretization. Therefore, even for very small resolutions, errors on the order of machine precision can easily be achieved. Indeed, we run this test with a mere 16 cells and achieve machine precision accuracy in the positions of the tracer particles.

4.2.2. Equilibrium Torus

Another simple flow is a torus in hydrostatic equilibrium about a black hole.¹¹ For this test, we use the initial conditions as described in Section 5.1. Briefly, we assume constant entropy and specific angular momentum with a tabulated SFHo EOS constructed by Steiner et al. (2013; see Section 5.1 for details). We use a relatively coarse grid: $96 \times 96 \times 64$ cells and $\sim 657,000$ tracer particles. We evolve the system for 500 gravitational times (GM_{BH}/c^3) with no seed magnetic field.

The continuum initial data is in equilibrium, but the numerical initial data is not. We allow the disk to relax toward

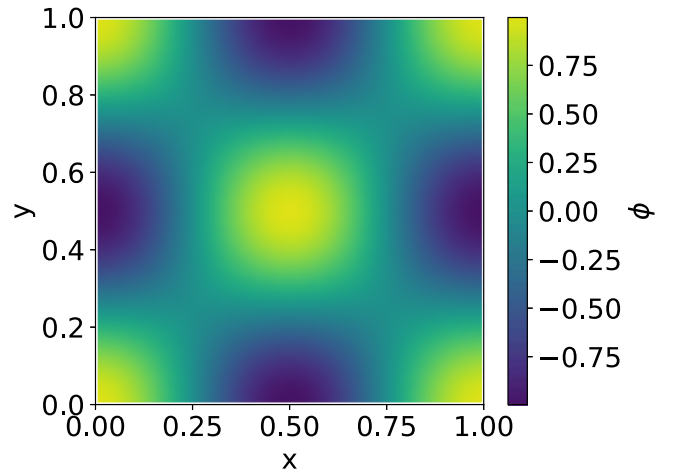


Figure 2. Two-dimensional slice of the solution to Equation (47) given initial data (Equation (49)) in 3D with periodic boundaries after one cycle. Our grid for this calculation was $64 \times 64 \times 64$.

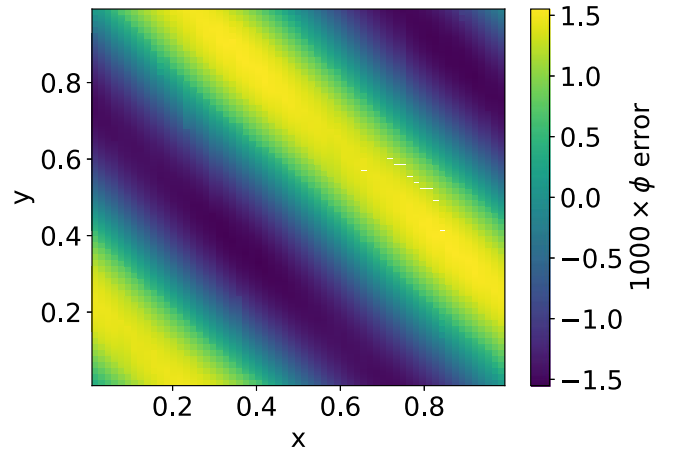


Figure 3. Pointwise error in the solution shown in Figure 2.

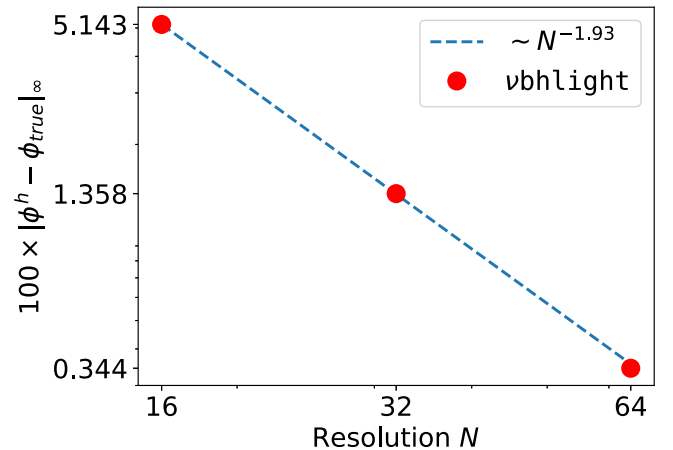


Figure 4. Convergence of the infinity norm of the error of the solution to Equation (47) given initial data (Equation (49)) in 3D with periodic boundaries after one cycle.

numerical equilibrium for 200 gravitational times, then select tracer particles within $1 \times GM_{\text{BH}}/c^2$ of the midplane of the disk. Figure 5 shows projections of a random selection's tracks of these tracer particles onto the xy -plane. The dynamical time in the inner region is shorter than in the outer region, so the

¹¹ The equilibrium torus is in an unstable equilibrium. Eventually a Papaloizou–Pringle instability will form. Fortunately, the growth time is long compared to the simulation time presented here (Papaloizou & Pringle 1984).

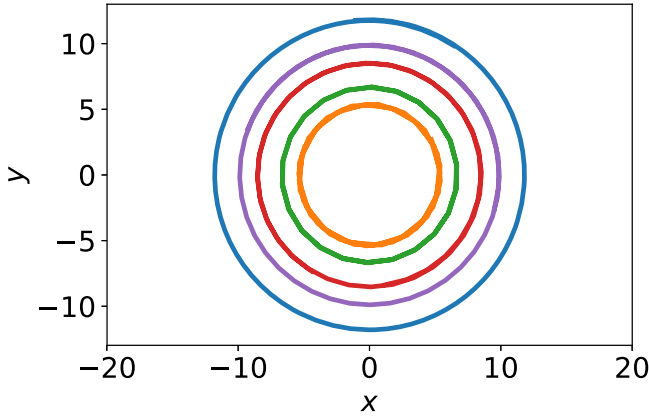


Figure 5. Tracks of tracer particles advected within an equilibrium torus.

innermost trace covers many orbits, while the outermost trace covers only one. Similarly, the outermost region is not yet in numerical equilibrium, hence why the track does not close.¹²

4.3. Fake Table Tests

To test our tabulated EOS reader, we tabulate the ideal gas law

$$P = (\Gamma - 1)u, \quad (50)$$

where Γ is the ratio of specific heats. Using this “fake” table, we can repeat tests presented in Ryan et al. (2015) in the absence of radiation. We perform the nonrelativistic linear waves and shock tube tests presented in Ryan et al. (2015).

The tables treat all quantities on a logarithmic scale. For Equation (50), the log of all thermodynamic quantities except sound speed is linear and the interpolation is exact, yielding identical results to an analytic EOS. The logarithm of the sound speed is linear at low velocities, but not at relativistic velocities. However, the tests we reproduce from Ryan et al. (2015) are nonrelativistic and so these nonlinearities are not present. Therefore, we expect agreement up to machine precision; indeed, we find this to be the case.

4.4. Artificial Neutrino Cooling

As a basic test of the coupling of neutrinos to matter, we study optically thin neutrino cooling in a simplified context. For this test, we choose to emit either only electron neutrinos or only electron antineutrinos. In each case, we define an emissivity of the form

$$j_{e,f} = Cy_f(Y_e)\chi([\nu_{\min}, \nu_{\max}]), \quad (51)$$

where C ensures the units and scale are appropriate,

$$\chi([\nu_{\min}, \nu_{\max}]) = \begin{cases} 1 & \text{if } \nu_{\min} \leq \nu \leq \nu_{\max} \\ 0 & \text{otherwise} \end{cases} \quad (52)$$

is the selection function, and $y_f(Y_e)$ is given by

$$y_f(Y_e) = \begin{cases} 2Y_e & \text{if emitting } \nu_e \\ 1 - 2Y_e & \text{if emitting } \bar{\nu}_e \\ 0 & \text{otherwise.} \end{cases} \quad (53)$$

Assuming a homogeneous and isotropic fluid at rest, this implies that the electron fraction Y_e and internal energy density u obey ordinary differential equations of the form

$$\partial_t Y_e = -A_C y_f(Y_e) \quad (54)$$

$$\text{and } \partial_t u = -B_C y_f(Y_e), \quad (55)$$

where

$$A_C = \frac{m_p}{h\rho} C \ln\left(\frac{\nu_{\max}}{\nu_{\min}}\right) \quad (56)$$

$$\text{and } B_C = C(\nu_{\max} - \nu_{\min}). \quad (57)$$

Equation (54) has a solution:

$$Y_e(t) = \begin{cases} 0 & \text{for } \nu_e \\ \frac{1}{2} + e^{-2A_C t} \left[(Y_e)_0 - \frac{1}{2} \right] & \text{for } \bar{\nu}_e, \end{cases} \quad (58)$$

where $(Y_e)_0 = Y_e(t=0)$. This implies that the electron fraction either exponentially decays to zero or exponentially approaches 1/2, depending on whether we emit electron neutrinos or electron antineutrinos. With this solution in hand, we can solve Equation (55) to find that

$$u(t) = u_0 + \frac{B_C}{A_C} (e^{-2A_C t} - 1) \begin{cases} (Y_e)_0 & \text{for } \nu_e \\ \frac{1}{2} - (Y_e)_0 & \text{for } \bar{\nu}_e, \end{cases} \quad (59)$$

where $u_0 = u(t=0)$.

In our tests, we choose

$$Y_e(t=0) = \begin{cases} \frac{1}{2} & \text{for } \nu_e, \\ 0 & \text{for } \bar{\nu}_e \end{cases} \quad (60)$$

so that Equation (58) reduces to

$$Y_e(t) = \begin{cases} -\frac{1}{2}e^{-2A_C t} & \text{for } \nu_e \\ \frac{1}{2}(1 - e^{-2A_C t}) & \text{for } \bar{\nu}_e \end{cases}$$

and Equation (59) reduces to

$$u(t) = u_0 + \frac{B_C}{2A_C} (e^{-2A_C t} - 1),$$

and $u(t)$ asymptotes to $u_0 - B_C/(2A_C)$. Figure 6 shows the electron fraction as a function of time for a gas cooled by electron neutrinos, and Figure 7 shows the analogous quantity for a gas cooled by electron antineutrinos. The energy density as a function of time looks identical whether we cool by electron neutrinos or electron antineutrinos. We plot this in Figure 8. In all cases, the agreement is good. A small deviation appears at late times, but since the plot is on a log scale, this deviation is extremely small.

¹² Since integration is not symplectic, we do not expect orbits to completely close, even with a perfectly relaxed disk. However, compared to the effect of disk relaxation, this effect is negligible and is not visible here.

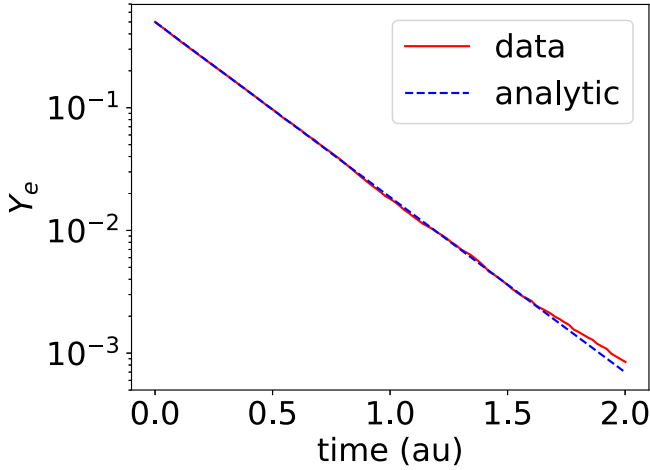


Figure 6. Electron fraction Y_e as a function of time for a homogeneous isotropic gas cooled by electron neutrinos. The solid line is the analytic solution, and the dashed line is the measured data. The agreement is very good.

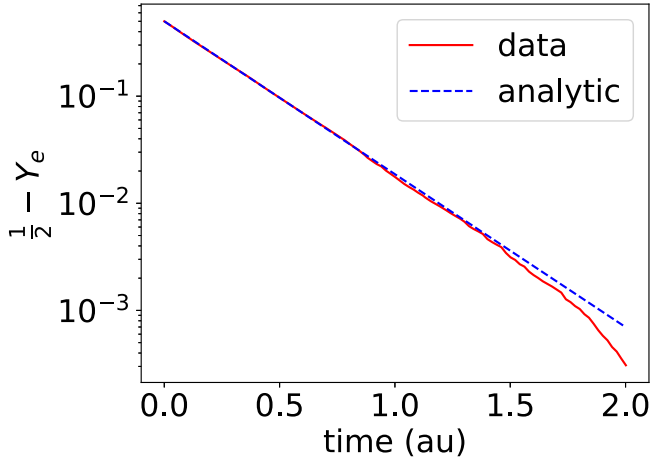


Figure 7. Electron fraction Y_e as a function of time for a homogeneous isotropic gas cooled by electron antineutrinos. The solid line is the analytic solution, and the dashed line is the measured data. The agreement is very good.

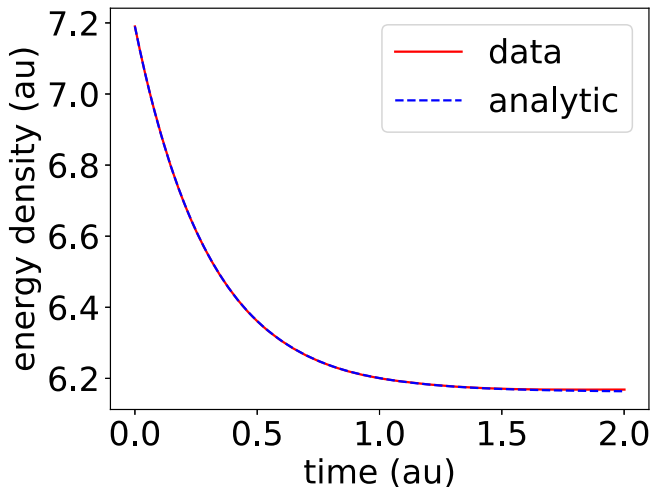


Figure 8. Energy density u as a function of time for a homogeneous isotropic gas cooled by neutrinos. The solid line is the analytic solution, and the dashed line is the measured data. The agreement is very good.

4.5. Artificial Single Scattering Events

Our procedure for biasing scattering on a per-interaction basis is a novel part of *νbhighlight*. Therefore, it is worth checking both that it works well and that it is worth the added complexity. We seek to test this here. In this test, we take a homogeneous, zero temperature gas and propagate a steady stream of heavy neutrinos traveling in the z -direction through it so that each neutrino traverses a scattering optical depth for the most likely scattering interaction of roughly $\Delta\tau = 1$. The optical depth for the less likely scattering interactions will be less than unity, with the least likely interaction significantly so. If the resolution is chosen so that the most likely scattering interaction is just barely well sampled, a naive biasing algorithm will undersample these less likely interactions.

After propagating the neutrinos, we investigate the directions of the neutrinos that have scattered exactly once. The probability distribution of directions traveled by these scattered neutrinos should match the total probability distribution formed by the sum of all differential scattering cross sections:

$$\frac{dN}{d\Omega} \sim \sum_p \frac{d\sigma_p}{d\Omega} \quad (61)$$

where $N(\theta, \phi)$ is the total number of heavy neutrinos traveling in the (θ, ϕ) direction, and $d\sigma_p/d\Omega$ is the differential cross section for a heavy neutrino scattering off of a gas particle of species p . We measure N integrated over the azimuthal direction:

$$\frac{dN}{d\theta}(\theta) \sim \sum_p \int d\phi \sin(\theta) \frac{d\sigma_p}{d\theta}. \quad (62)$$

For the purpose of this test, we introduce three fake particles, with three fake, anisotropic, elastic scattering kernels:

$$\frac{d\sigma_i}{d\Omega} = \sigma_0(4i + 1)(1 + \mu^{2i+1}), \quad i = 0, 1, 2, \quad (63)$$

where $\mu = \cos(\theta)$. These interactions have different total cross sections and, thus, different probabilities that an individual neutrino will scatter via a given process. However, if all processes are well sampled, we should be able to measure a probability distribution that matches Equation (62).

We perform this experiment in two ways. First, we use a single global bias that modifies scattering probability uniformly across all interactions. For a resolution that marginally well-samples the most likely interaction ($i = 2$), the less likely interactions ($i = 0, 1$) will be undersampled. Second, we bias each scattering interaction individually, as described in Section 3.2.3. This second approach should more evenly sample all interactions for a given resolution. In both cases, we use the same number of superneutrinos (roughly 10^6) and set the biases such that the same number of unscattered superneutrinos scatters each time step (roughly 4×10^4).

We show our results in Figure 9. The area of the blue shaded region is the integral $\int (dN/d\Omega)d\Omega$ of Equation (61), meaning the boundary of the shaded region is given by Equation (63). The green dashed curve is the probability distribution of superneutrinos measured when the experiment is performed with a single global bias. The red solid curve is the probability distribution measured when the experiment is performed with per-interaction biases.

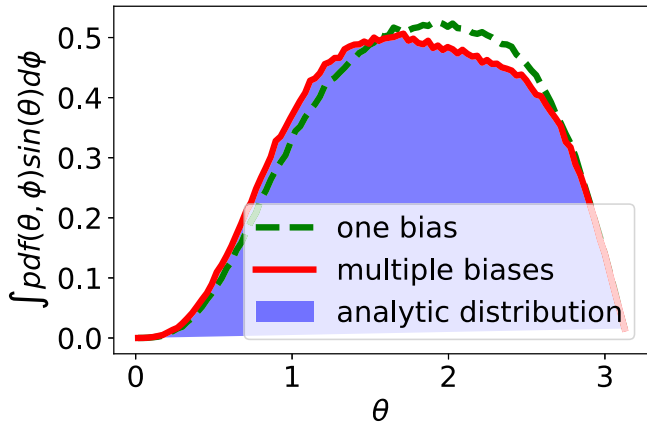


Figure 9. Distribution of scattered physical neutrinos as a function of angle θ . The blue shaded region represents the integral of the analytic solution. The green dashed line is measured data with a single global bias parameter. The red solid line is measured data with multiple per-scattering-process biases. Scattering with per-process biases matches the analytic solution very well, while scattering with a single global bias undersamples some processes and oversamples others.

When global biases are used, $d\sigma_0/d\Omega$ and $d\sigma_1/d\Omega$ are undersampled with respect to $d\sigma_2/d\Omega$. But when per-interaction biases are used, the agreement with Equation (62) is quite good. This indicates both the necessity and efficacy of per-interaction biases.

4.6. 2D Lepton Transport

A major motivation for treating neutrino radiation accurately is the fact that neutrinos can carry a lepton number from one place to another. In the context of an accretion disk, this means leptons—and thus the electron fraction—can be transported from one part of the disk to another.

To demonstrate this capability in *νbhlight*, we perform the following simple 2D test. Consider a gas in a 2D periodic box:

$$(x, y) \in [-1, 1]^2. \quad (64)$$

The gas is at a constant density and temperature,

$$\rho = 10^{10} \text{ g cm}^{-3}, \quad (65)$$

$$T = 2.5 \text{ MeV}, \quad (66)$$

and a piecewise-constant electron fraction defined by

$$Y_e = \begin{cases} 0.1 & \text{if } (x, y) \in [-0.75, -0.25]^2 \\ 0.35 & \text{if } (x, y) \in [0.25, 0.75]^2 \\ 0.225 & \text{otherwise,} \end{cases} \quad (67)$$

so that there is one “hot spot” of Y_e and one “cold spot.” The hot and cold spot regions are separated from the rest of the gas by membranes that are impermeable by the gas but through which neutrinos can travel freely. In this way, the gas does not evolve due to pressure gradients.

Over time, as neutrinos are emitted and absorbed, the electron fractions in the hot spot and the cold spot will come to equilibrium with each other. Indeed, the gas itself will come into equilibrium with the radiation field. Figure 10 shows the electron fraction as a function of space for three times. Figure 11 shows the evolution of the electron fraction as a function of time. The average electron fraction experiences an early transient as leptons are carried into the radiation field but

then remains stable. The hot spot and cold spot converge to the average exponentially with time. The final electron fraction is not the average Y_e in the initial condition.

4.7. Code Comparisons

The tests described in Sections 4.4 and 4.5 use artificial emissivities and scattering cross sections. This has the advantage of permitting an analytic solution against which we can compare. However, it has the significant disadvantage of being unphysical. We would also like to test the performance of our physical emissivities and absorption opacities.

To this end, we compare our code to the supernova code FORNAX (Skinner et al. 2019) in two simple test cases. The two codes are designed for different scenarios and use significantly different methods. *νbhlight* is fully general relativistic, whereas FORNAX uses nonrelativistic dynamics and an approximate treatment for gravity. *νbhlight* uses Monte Carlo transport for neutrinos, while FORNAX uses a multigroup moment formalism with the M1 closure model (Castor 2004). Some care is thus required to choose test cases where both codes converge to the same, physically correct, solution.

We, therefore, use a simple 0D setup. We use a homogeneous and isotropic gas at rest on a periodic domain in Minkowski space. We also use the same EOS: SFHo by Steiner et al. (2013). This eliminates discrepancies due to treatment of the gas. We use the same emission and absorption opacities, as presented in Burrows et al. (2006), Skinner et al. (2019), and provided by A. Burrows (2018, private communication). Since the scattering cross sections are different between the codes, we disable scattering for these tests. Moreover, by studying only homogeneous, isotropic radiation, we enter a regime where the M1 closure model is valid.

In both our comparison tests, we use the following initial conditions for the gas:

$$\rho_0(t=0) = 10^9 \text{ g cm}^{-3}, \quad (68)$$

$$T(t=0) = 2.5 \text{ MeV}, \quad (69)$$

$$Y_e(t=0) = 0.1, \quad (70)$$

which roughly mimic conditions one might encounter in a neutrino-driven accretion flow. We run each calculation for total duration of 0.5 s. We assume that there is no radiation at the initial time. In both cases, we run FORNAX with 200 energy groups and energies ranging from 1 to 300 MeV. We run *νbhlight* with a target number of 10^5 superneutrinos, which can have energies in the same range as in FORNAX.

4.7.1. Optically Thin Cooling

In this test, we enable emissivity but disable absorption and scattering. Traces of an electron fraction and temperature are shown for both FORNAX and *νbhlight* in Figure 12. The cooling rate is a steep function of temperature. As the gas cools rapidly, the electron fraction changes rapidly before reaching equilibrium.

The agreement between FORNAX and *νbhlight* is at the percent level, as shown in Figure 13. Given that the codes use dramatically different methods, this agreement is quite satisfactory for the problem of interest.

4.7.2. Thermalization

In this test, we enable both emission and absorption but disable scattering. The goal is to watch as the gas and the

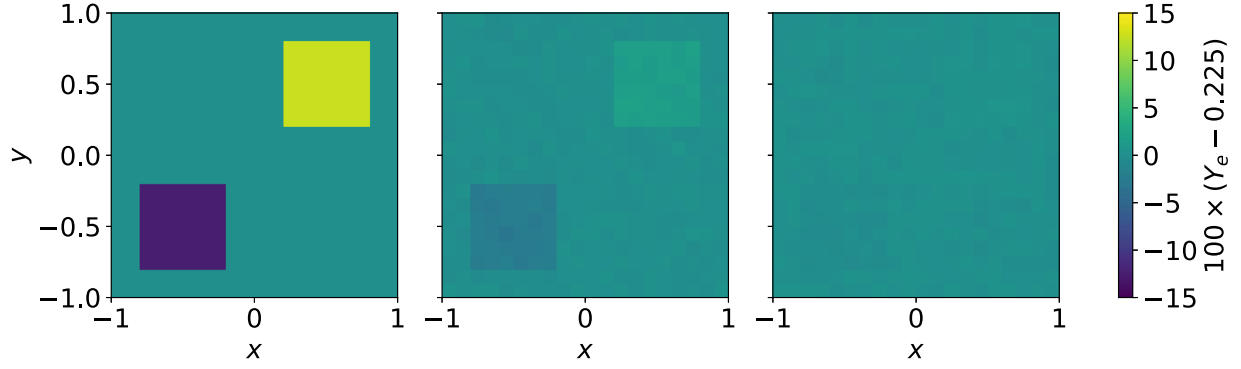


Figure 10. Neutrinos equilibrate electron fraction between a hot spot and a cold spot as time passes. Left: the system at the initial time. Center: the system after ~ 5 ms. Right: The system after ~ 10 ms.

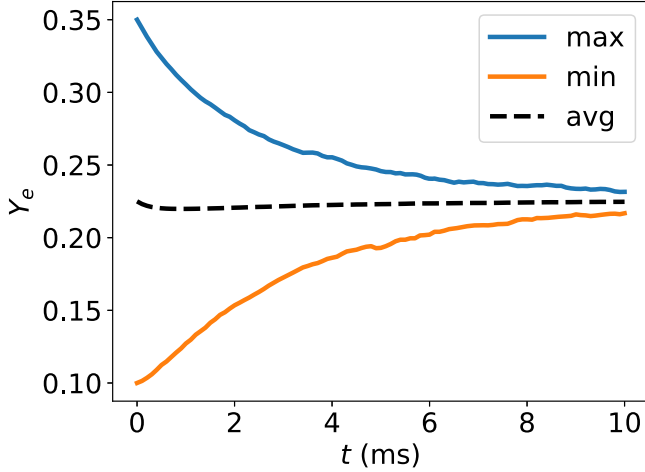


Figure 11. Electron fraction as a function of time for the hot spot (blue), the cold spot (orange), and the remainder of the gas (black). The average electron fraction experiences an early transient as leptons are carried into the radiation field but then remains stable. The hot spot and cold spot converge to the average exponentially with time.

radiation reach thermal equilibrium. We plot the electron fraction and the temperature for both `FORNAX` and `νbhlight` in Figure 14. The electron fraction changes very rapidly, but the cooling rate is subdued thanks to absorption.

`νbhlight` and `FORNAX` again agree within about a percent, as shown in Figure 15. Again, given that the codes use dramatically different methods, this agreement is quite good.

5. Post-merger Disk

As a demonstration of `νbhlight`'s capabilities, we perform a fully 3D neutrino radiation GRMHD simulation of a representative accretion disk that formed from a compact binary merger. Although we do not perform a detailed analysis, we believe our qualitative results compellingly demonstrate both the capabilities of our code and a need for those capabilities.

5.1. Disk Setup

We set up an axisymmetric disk in hydrostatic equilibrium on a Kerr background.¹³ We demand that our disk have

¹³ We perform the setup in Boyer–Lindquist coordinates but transition to the modified Kerr–Schild coordinates described in (Gammie et al. (2003)) for the evolution. For a detailed discussion of these various coordinate systems, see Poisson (2004) and references therein.

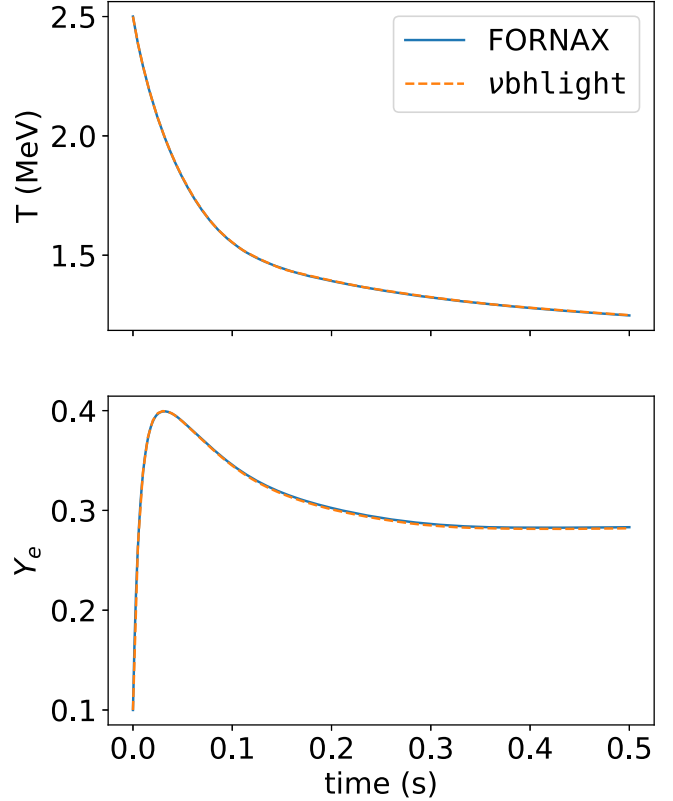


Figure 12. Temperature T and electron fraction Y_e for the optically thin cooling comparison between `νbhlight` and `FORNAX`. The electron fraction rapidly grows as the gas cools.

constant fixed specific entropy s , specific angular momentum l , and electron fraction Y_e . Under these conditions, the relativistic Euler equations can be written as an exterior differential system, which can be integrated along characteristics for the specific enthalpy h , as derived in Fishbone & Moncrief (1976).

Figure 16 shows the specific enthalpy as a function of $\log_{10} \rho$ and $\log_{10} T$ for the Hempel SFHo (Hempel et al. 2012) EOS with the fixed electron fraction $Y_e = 0.1$. Overlaid on top of the heat map are contours of constant entropy. To construct a constant entropy disk, we find one of these contours and move along it. Each contour represents a relationship between $\log_{10} \rho$ and $\log_{10} T$.

The exterior differential system for the enthalpy introduces several constants of integration. These are set by the innermost radius of the disk, R_{in} ; the radius of maximum pressure; R_{max} ;

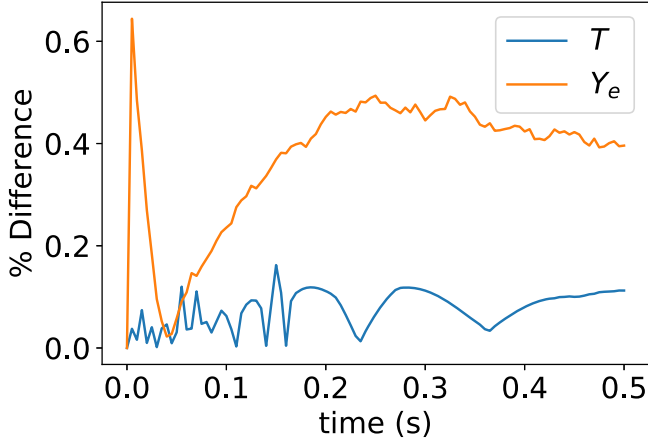


Figure 13. Percent difference in temperature T and electron fraction Y_e for the optically thin cooling comparison between ν bhlight and FORNAX.

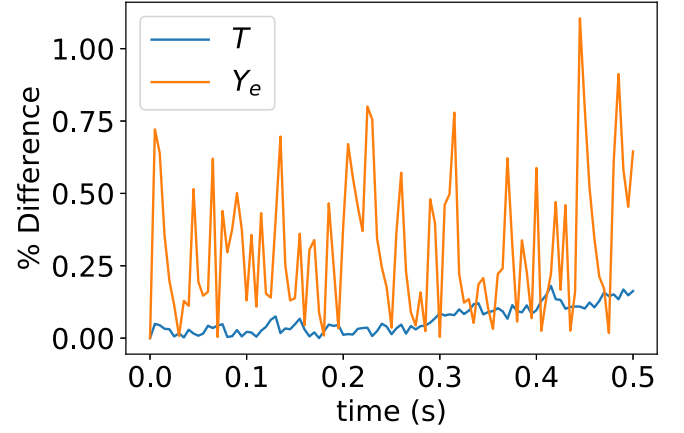


Figure 15. Percent difference in temperature T and electron fraction Y_e for the thermal comparison between ν bhlight and FORNAX.

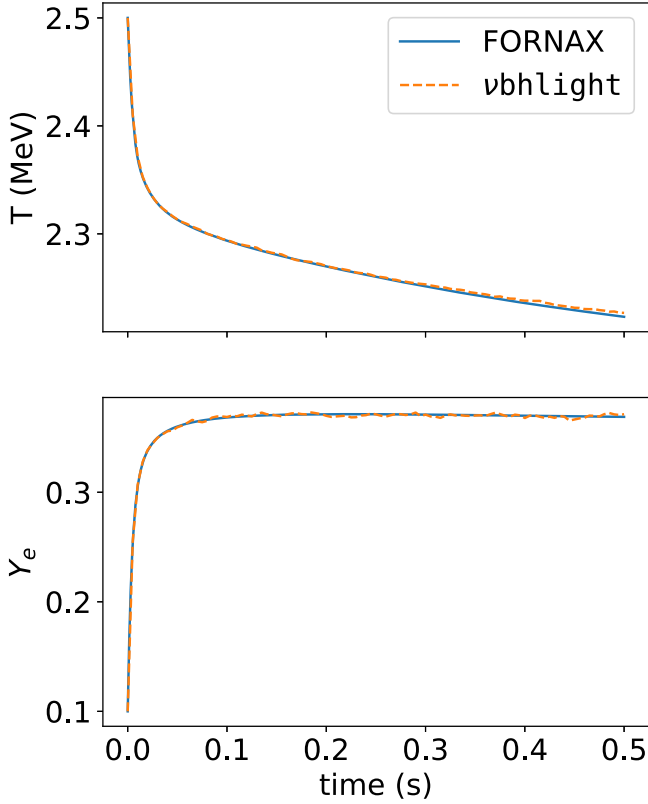


Figure 14. Temperature T and electron fraction Y_e for the thermal equilibrium comparison between ν bhlight and FORNAX. The electron fraction rapidly grows as the gas cools before reaching equilibrium.

and the limit,

$$h_0(s, Y_e) = \lim_{P \rightarrow 0} h(s, Y_e), \quad (71)$$

for a given entropy s and electron fraction Y_e . For ideal gases, $h_0 \geq c$. However, this is not the case for more general equations of state. The only constraint is that $h \geq 0$, as required by the weak energy condition. We plot $h - c^2$ versus pressure for $s = 4 k_b/\text{baryon}$ and $Y_e = 0.1$ in Figure 17. Note the offset along the y-axis.

We initialize the disk with a uniform, weak, purely poloidal magnetic field with a minimum ratio of gas to magnetic

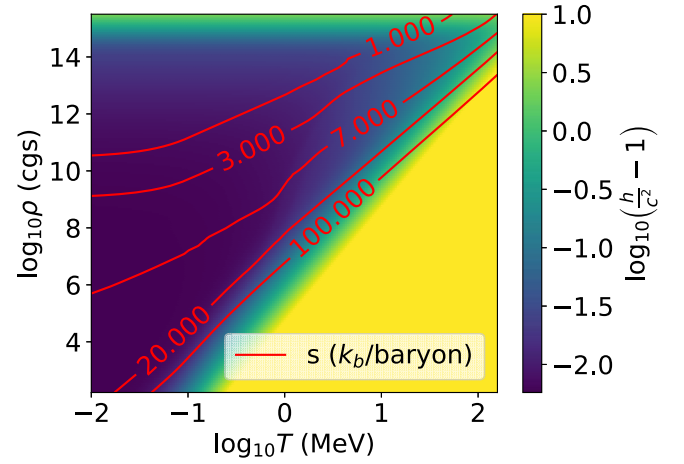


Figure 16. Contours of constant entropy (in units of k_b/baryon) superposed on a plot of specific enthalpy in terms of $\log_{10} \rho$ and $\log_{10} T$ for the SFHo EOS. Here, we assume a constant electron fraction of $Y_e = 0.1$.

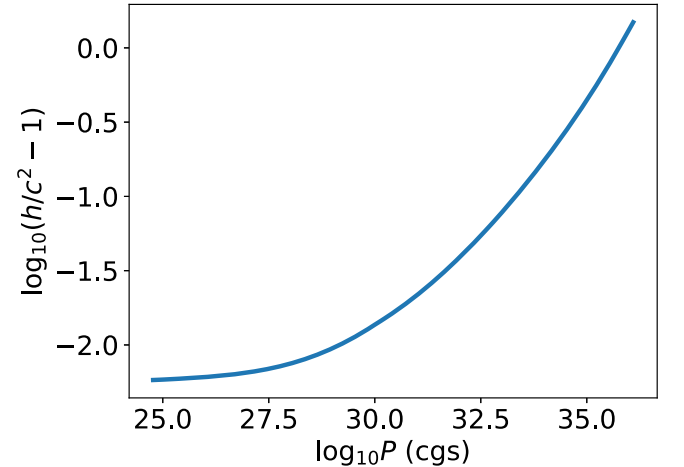


Figure 17. Specific enthalpy vs. pressure for $s = 4 k_b/\text{baryon}$ and $Y_e = 0.1$. Note the offset along the y-axis. The specific enthalpy is not identically equal to the speed of light for small pressures.

pressure:

$$\beta = 2 \frac{P}{B^2}, \quad (72)$$

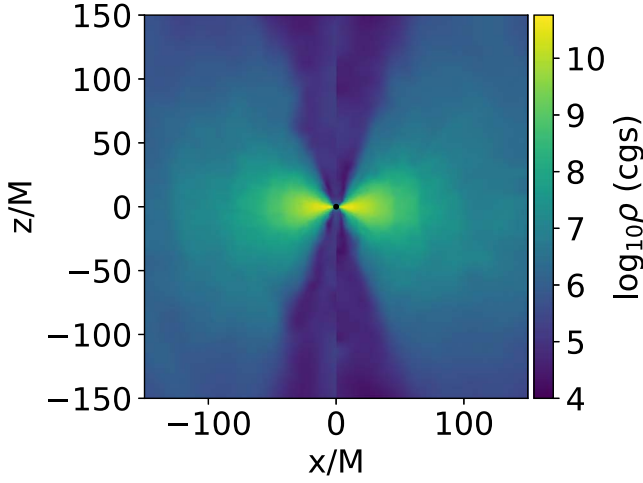


Figure 18. Density of the disk-outflow system in the xz -plane at time $10^4 \times GM_{\text{BH}}/c^3$.

Table 2
Parameters of the Initial Data for Our Black Hole–Disk System

Parameter	Value	Units
M_{BH}	2.80	M_{\odot}
a_{BH}	0.80	$J_{\text{BH}}/M_{\text{BH}}^2$
s	4.00	k_b/baryon
Y_e	0.10	$n_e/(n_e + n_p)$
M_{disk}	0.05	M_{\odot}
R_{in}	3.70	M_{BH}
R_{max}	9.03	M_{BH}

Note. M_{BH} and a_{BH} are the mass and spin of the black hole, respectively. s and Y_e are the entropy and the electron fraction, which are assumed to be constant throughout the initial disk. M_{disk} is the mass of the disk. R_{in} is the inner radius of the disk, and R_{max} is the radius of maximum pressure. We set $G = c = 1$.

Table 3
Numerical Parameters Used for the Post-merger Disk Calculation

Parameter	Value
N_1	192
N_2	128
N_3	66
N_{ν}/cell	5
N_t	1.6×10^6
R_{out}	$10^3 M_{\text{BH}}$

Note. N_1 , N_2 , and N_3 are the numbers of cells in the r , θ , and ϕ directions, respectively. N_{ν}/cell is the number of supernutrinos per cell. N_t is the number of tracer particles. R_{out} is the radius of the outer boundary of the simulation with $G = c = 1$.

which acts as the seed field for the magneto-rotational instability (Velikhov 1959). We summarize our parameter choices for our disk in Table 2. We summarize the numerical parameters used in Table 3.

5.2. Results

We run our simulation for $10,000 GM_{\text{BH}}/c^3$, or ~ 138 milliseconds. Figures 18 and 19 show the density of the disk at late times. Neutrinos can carry a lepton number and vary the

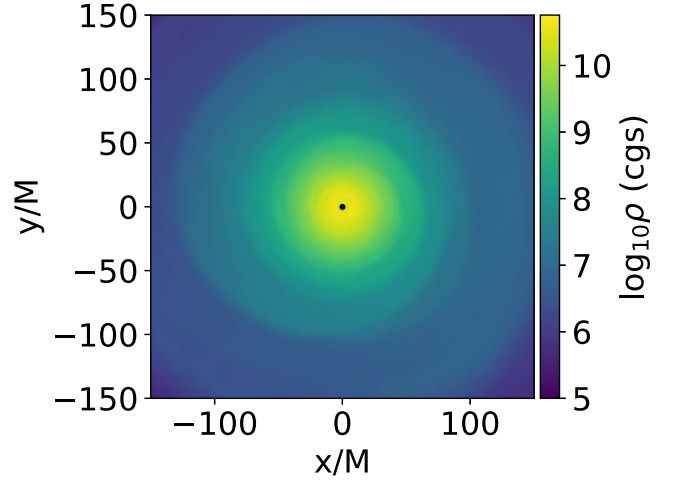


Figure 19. Density of the disk-outflow system in the xy -plane at time $10^4 \times GM_{\text{BH}}/c^3$.

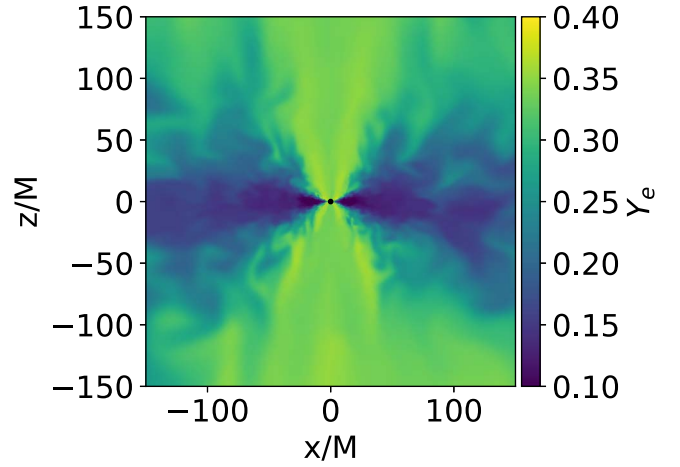


Figure 20. Electron fraction of material in the disk-outflow system in the xz -plane at time $10^4 \times GM_{\text{BH}}/c^3$. The composition of the material in the polar regions is untrustworthy, as this is jet material.

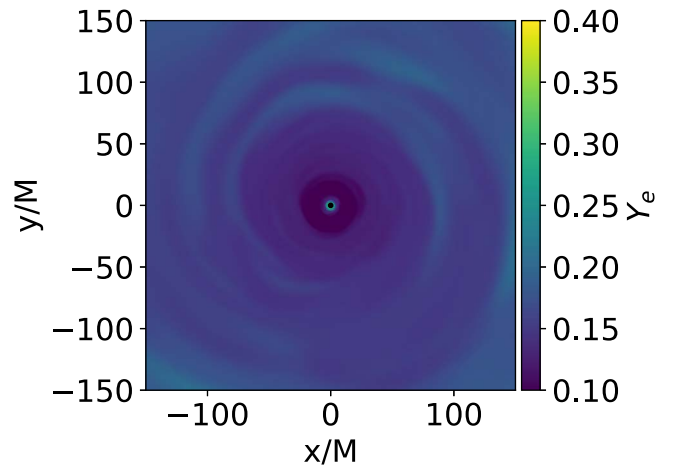


Figure 21. Electron fraction of material in the disk-outflow system in the xy -plane at time $10^4 \times GM_{\text{BH}}/c^3$.

electron fraction as a function of space and time. Figures 20 and 21 show the electron fraction of the disk-wind system at late times. The core of the disk still has a very low electron fraction—close to $Y_e \sim 0.1$. However, the outflow has a

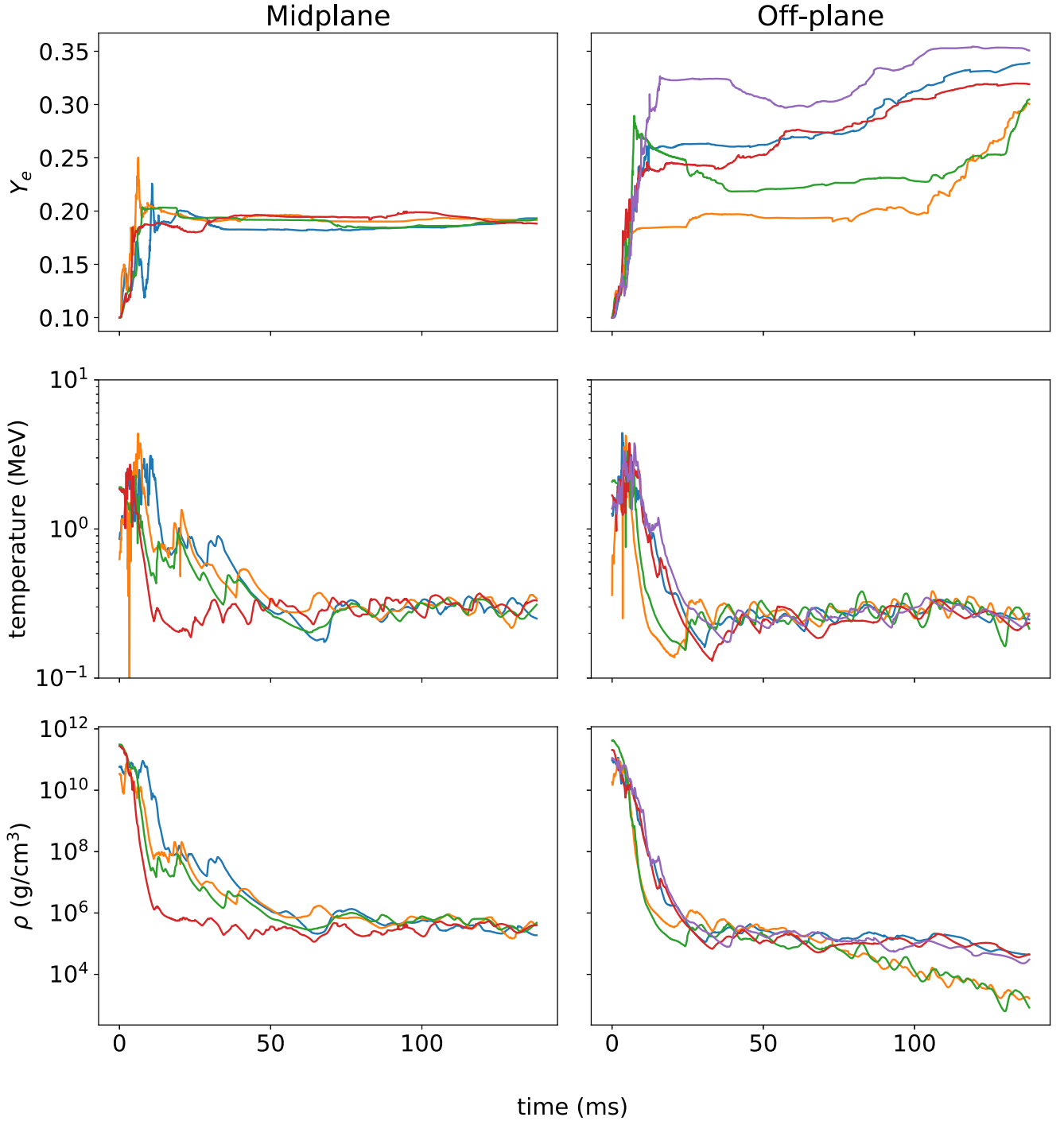


Figure 22. Density ρ , temperature T , and electron fraction Y_e as a function of time for five characteristic tracers each for material in the midplane (left) and material near Boyer–Lindquist $\theta \sim \pi/3$ for tracers at $r \geq 100M$ at time $10^4 \times GM_{\text{BH}}/c^3$.

composition that varies significantly in space. Material in the equatorial plane still has a low electron fraction, near $Y_e \sim 0.2$. However, material far from the midplane has an electron fraction as large as $Y_e \sim 0.3$.

We make these qualitative observations more quantitative by examining tracer data. For this analysis, we use tracers that have reached radii greater than a fixed extraction radius of $r_{\text{min}} = 100$ at time $10,000 GM_{\text{BH}}/c^3$. We plot the density,

temperature, and electron fraction as a function of time for several characteristic tracer particles both in the midplane and off-plane in Figure 22. Although we do not calculate yields here, these kinds of tracers may be used as input into a nuclear reaction network to calculate yields. Although not conclusive, we believe these results are highly suggestive that realistic neutrino transport is required to accurately model these systems. We will pursue this detailed modeling in future work.

6. Concluding Thoughts

We have developed the capacity to accurately study neutrino-driven accretion flows via Monte Carlo methods. We validated the accuracy of our approach via a variety of code tests, as discussed in Section 4. Moreover, we demonstrated this capability by performing a fully 3D general relativistic neutrino radiation-magnetohydrodynamics calculation of a representative black hole accretion-disk system formed by a compact binary merger. With realistic neutrino transport active, we observe a rich phenomenology of the wind morphology and composition.

Since we will observe many more compact binary mergers in the coming years, accurately modeling these systems, and their remnants, is of critical importance. We believe *νbhlight* represents a key tool in this modeling effort. In the future, we will use *νbhlight* to investigate the morphology of the disk-wind system in the context of multimessenger observables.

The authors thank Chris Fryer, Francois Foucart, Daniel Siegel, Oleg Korobkin, Jonas Lippuner, and Roseanne Cheng for many valuable discussions. We are especially grateful to Adam Burrows for providing us with neutrino opacity tables and explaining how these tables are produced (A. Burrows 2018, private communication).

We acknowledge support from the U.S. Department of Energy Office of Science and the Office of Advanced Scientific Computing Research via the Scientific Discovery through Advanced Computing (SciDAC4) program and Grant DE-SC0018297




This work was supported by the US Department of Energy through the Los Alamos National Laboratory. Additional funding was provided by the Laboratory Directed Research and Development Program and the Center for Nonlinear Studies at Los Alamos National Laboratory under project No. 20170508DR. Los Alamos National Laboratory is operated by Triad National Security, LLC, for the National Nuclear Security Administration of U.S. Department of Energy (contract No. 89233218CNA000001).

This research used resources provided by the Los Alamos National Laboratory Institutional Computing Program, which is supported by the U.S. Department of Energy National Nuclear Security Administration under contract No. 89233218CNA000001.

This article is cleared for unlimited release: LA-UR-19-20336.

We are grateful to the countless developers contributing to open source projects on which we relied on in this work, including Python (Rossum 1995), numpy and scipy (Jones et al. 2001; van der Walt et al. 2011), and Matplotlib (Hunter 2007).

ORCID iDs

Jonah M. Miller  <https://orcid.org/0000-0001-6432-7860>
Ben. R. Ryan  <https://orcid.org/0000-0001-8939-4461>
Joshua C. Dolence  <https://orcid.org/0000-0003-4353-8751>

References

Abbott, B. P., Abbott, R., Abbott, T. D., et al. 2017a, *ApJL*, **848**, L12
Abbott, B. P., Abbott, R., Abbott, T. D., et al. 2017b, *PhRvL*, **119**, 161101
Abramowicz, M. A., & Fragile, P. C. 2013, *LRR*, **16**, 1
Aufderheide, M. B., Fushiki, I., Fuller, G. M., & Weaver, T. A. 1994, *ApJ*, **424**, 257
Balbus, S. A., & Hawley, J. F. 1991, *ApJ*, **376**, 214
Blandford, R. D., & Znajek, R. L. 1977, *MNRAS*, **179**, 433
Blinnikov, S. I., Novikov, I. D., Perevodchikova, T. V., & Polnarev, A. G. 1984, *SvAL*, **10**, 177

Bovard, L., & Rezzolla, L. 2017, *CQGr*, **34**, 215005
Bruenn, S. W. 1985, *ApJS*, **58**, 771
Bruenn, S. W., & Mezzacappa, A. 1997, *PhRvD*, **56**, 7529
Burrows, A., Reddy, S., & Thompson, T. A. 2006, *NuPhA*, **777**, 356
Canfield, E., Howard, W. M., & Liang, E. P. 1987, *ApJ*, **323**, 565
Castor, J. 2004, *Radiation Hydrodynamics*, Radiation Hydrodynamics (Cambridge: Cambridge Univ. Press)
Côté, B., Fryer, C. L., Belczynski, K., et al. 2018, *ApJ*, **855**, 99
Dolence, J. C., Gammie, C. F., Mościbrodzka, M., & Leung, P. K. 2009, *ApJS*, **184**, 387
Duan, H., Friedland, A., McLaughlin, G. C., & Surman, R. 2011, *JPhG*, **38**, 035201
Eichler, D., Livio, M., Piran, T., & Schramm, D. N. 1989, *Natur*, **340**, 126
Fernández, R., & Metzger, B. D. 2016, *ARNPS*, **66**, 23
Fernández, R., Tchekhovskoy, A., Quataert, E., et al. 2019, *MNRAS*, **482**, 3373
Fishbone, L. G., & Moncrief, V. 1976, *ApJ*, **207**, 962
Foucart, F. 2018, *MNRAS*, **475**, 4186
Foucart, F., Deaton, M. B., Duez, M. D., et al. 2014, *PhRvD*, **90**, 024026
Foucart, F., O'Connor, E., Roberts, L., et al. 2015, *PhRvD*, **91**, 124021
Freedman, D. Z. 1974, *PhRvD*, **9**, 1389
Fuller, G. M., Fowler, W. A., & Newman, M. J. 1982, *ApJ*, **252**, 715
Gammie, C. F., McKinney, J. C., & Tóth, G. 2003, *ApJ*, **589**, 444
Harten, A., Lax, P. D., & van Leer, B. 1983, *SIAMR*, **25**, 35
Hempel, M., Fischer, T., Schaffner-Bielich, J., & Liebendörfer, M. 2012, *ApJ*, **748**, 70
Horowitz, C. J. 1997, *PhRvD*, **55**, 4577
Hossein Nouri, F., Duez, M. D., Foucart, F., et al. 2018, *PhRvD*, **97**, 083014
Hunter, J. D. 2007, *CSE*, **9**, 90
Jaroszynski, M. 1996, *A&A*, **305**, 839
Jones, E., Oliphant, T., Peterson, P., et al. 2001, *SciPy: Open Source Scientific Tools for Python*, <http://www.scipy.org/>
Lattimer, J. M., Mackie, F., Ravenhall, D. G., & Schramm, D. N. 1977, *ApJ*, **213**, 225
Lattimer, J. M., & Schramm, D. N. 1976, *ApJ*, **210**, 549
Leinson, L., Oraevsky, V., & Semikoz, V. 1988, *PhLB*, **209**, 80
Li, L.-X., & Paczyński, B. 1998, *ApJL*, **507**, L59
Liu, X.-D., Osher, S., & Chan, T. 1994, *JCoPh*, **115**, 200
Martí, J. M., Ibáñez, J. M., & Miralles, J. A. 1991, *PhRvD*, **43**, 3794
Metzger, B. D., Zinner, N. T., Martínez-Pinedo, G., et al. 2010, *MNRAS*, **406**, 2650
Mignone, A., & McKinney, J. C. 2007, *MNRAS*, **378**, 1118
Miralles, J. A., van Riper, K. A., & Lattimer, J. M. 1993, *ApJ*, **407**, 687
Mooley, K. P., Deller, A. T., Gottlieb, O., et al. 2018, *arXiv:1806.09693*
Narayan, R., Paczyński, B., & Piran, T. 1992, *ApJL*, **395**, L83
O'Connor, E., & Ott, C. D. 2010a, *CQGr*, **27**, 114103
O'Connor, E., & Ott, C. D. 2010b, *Stellar Collapse: Microphysics*, <https://stellarcollapse.org/equationofstate>
Papaloizou, J. C. B., & Pringle, J. E. 1984, *MNRAS*, **208**, 721
Poisson, E. 2004, *A Relativist's Toolkit: The Mathematics of Black-Hole Mechanics* (Cambridge: Cambridge Univ. Press)
Richers, S., Kasen, D., O'Connor, E., Fernandez, R., & Ott, C. D. 2015, *ApJ*, **813**, 38
Rossum, G. 1995, *Python Reference Manual*, CWI Rep. CS-R9526, (Amsterdam: Centrum voor Wiskunde en Informatica)
Ryan, B. R., Dolence, J. C., & Gammie, C. F. 2015, *ApJ*, **807**, 31
Sekiguchi, Y., Kiuchi, K., Kyutoku, K., & Shibata, M. 2015, *PhRvD*, **91**, 064059
Siegel, D. M., Barnes, J., & Metzger, B. D. 2018, *arXiv:1810.00098*
Siegel, D. M., & Metzger, B. D. 2018, *ApJ*, **858**, 52
Skinner, M. A., Dolence, J. C., Burrows, A., Radice, D., & Vartanyan, D. 2019, *ApJS*, **241**, 7
Soares-Santos, M., et al. 2017, *ApJL*, **848**, L16
Steiner, A. W., Hempel, M., & Fischer, T. 2013, *ApJ*, **774**, 17
Tanvir, N. R., Levan, A. J., González-Fernández, C., et al. 2017, *ApJL*, **848**, L27
Tchekhovskoy, A., McKinney, J. C., & Narayan, R. 2007, *MNRAS*, **379**, 469
Toro, E. 2013, *Riemann Solvers and Numerical Methods for Fluid Dynamics: A Practical Introduction* (Berlin: Springer)
Tóth, G. 2000, *JCoPh*, **161**, 605
Tubbs, D. L., & Schramm, D. N. 1975, *ApJ*, **201**, 467
van der Walt, S., Colbert, S. C., & Varoquaux, G. 2011, *CSE*, **13**, 22
Velikhov, E. 1959, *ZhETF*, **36**, 5
Wald, R. 2010, *General Relativity* (Chicago, IL: Univ. Chicago Press)